Physics – Uspekhi **60** (4) 419 – 429 (2017)

CONFERENCES AND SYMPOSIA

PACS numbers: **74.25.–q**, 74.25.nd, 74.25.Ha, **74.45.+c**, 74.70.Xa

100th ANNIVERSARY OF THE BIRTH OF V L GINZBURG

On the structure of the superconducting order parameter in high-temperature Fe-based superconductors

T E Kuzmicheva, A V Muratov, S A Kuzmichev, A V Sadakov, Yu A Aleshchenko, V A Vlasenko, V P Martovitsky, K S Pervakov, Yu F Eltsev, V M Pudalov

DOI: https://doi.org/10.3367/UFNe.2016.10.038002

Contents

Abstract. We discuss the synthesis, characterization, and comprehensive study of Ba-122 single crystals with various substitutions and various superconducting transition temperatures. We use five complementary techniques to obtain a self-consistent set of data on the superconducting properties of Ba-122. A major conclusion of our work is the coexistence of two superconducting condensates differing in the electron–boson coupling strength. The two gaps that develop in distinct Fermi surface sheets are nodeless in the k_xk_y plane and exhibit s-wave symmetry; the two-band model suffices for the description of the main parameters of the superconducting state. A moderate interband coupling and a considerable Coulomb repulsion in the description of the two-gap superconducting state of barium pnictides favor the s^{++} model.

Keywords: multi-gap superconductors, iron pnictides, specific heat, London penetration depth, Andreev spectroscopy, optics

T E Kuzmicheva, A V Muratov, A V Sadakov, V A Vlasenko, V P Martovitsky, Yu F Eltsev Lebedev Physical Institute, Russian Academy of Sciences, Leninskii prosp. 53, 119991 Moscow, Russian Federation
E-mail: kute@sci.lebedev.ru
S A Kuzmichev Lomonosov Moscow State University, Faculty of Physics, Leninskie gory 1, str. 2 119991 Moscow, Russian Federation; Lebedev Physical Institute, Russian Academy of Sciences, Leninskii prosp. 53, 119991 Moscow, Russian Federation
Yu A Aleshchenko Lebedev Physical Institute, Russian Academy of Sciences, Leninskii prosp. 53, 119991 Moscow, Russian Federation; National Research Nuclear University MEPhI (Moscow Engineering Physics Institute), Kashirskoe shosse 31, 115409 Moscow, Russian Federation
K S Pervakov Lebedev Physical Institute, Russian Academy of Sciences, Leninskii prosp. 53, 119991 Moscow, Russian Federation; International Laboratory of High Magnetic Field and Low Temperatures, ul. Gajowicka 95, 53-421 Wroclaw, Poland
V.M. Pudalov Lebedev Physical Institute, Russian Academy of Sciences, Leninskii prosp. 53, 119991 Moscow, Russian Federation; National Research University: Higher School of Economics, ul. Myasnitskaya 20, 101000 Moscow, Russian Federation

Received 7 December 2016
Uspekhi Fizicheskikh Nauk **187** (4) 450 – 462 (2017)
DOI: https://doi.org/10.3367/UFNr.2016.10.038002
Translated by T E Kuzmicheva; edited by A M Semikhatov

1. Introduction

Unconventional superconductivity in quasi-two-dimensional iron compounds discovered in 2008 [1] is undoubtedly a challenging issue in condensed matter physics. Demonstrating critical temperatures T_c up to 56 K for bulk SmOFeAs [2], and up to 100 K in monolayer FeSe [3], as well as possessing huge critical fields as high as 200 T [4], pnictides and selenides have potential in wide applications [5, 6]. Being antiferromagnetic metals with a spin-density wave (SDW) ground state in stoichiometric composition, the majority of iron pnictides and selenides become superconductive via electron or hole doping. However, the two exceptions are the well-known LiFeAs [7] and the recently discovered ThNOFeAs, whose stoichiometric phases are nonmagnetic. The latter compound has a structure similar to oxyarsenides (the so-called 1111 system) and has a comparable $T_c \approx 30$ K [8]. We note that the Fermi energy is rather low for iron-based superconductors. For example, for the 'driving' band near the Γ point, the Fermi energy relative to the bottom of the band is about 0.2 eV [9].

Compared to other iron superconductors, $BaFe_{2-x}Ni_xAs_2$ and $Ba_{1-x}K_xFe_2As_2$, representative members of the so-called

Ba-122 family, are attractive to the research community due to both moderate T_c (up to 38 K) and the rather easy growth of large and high-quality single crystals with variable substitution. Band-structure calculations [10] have shown several Fe 3d orbital bands crossing the Fermi level, forming cylinder-like Fermi surface sheets slightly warped in the *c*-axis direction, hole-like around the Γ point, and electron-like around the M point. The presence of multiple superconducting condensates below T_c and the corresponding forbidden energy bands (superconducting gaps) have been unambiguously confirmed, both theoretically and experimentally [11, 12].

To explain the underlying pairing mechanism in Fe-based superconductors, three basic models have been presented. One of them, the s^{++} model, predicts a strong intraband coupling and two competing pairings — via spin fluctuations and via orbital fluctuations enhanced by phonons [13, 14]. This competition could lead to an anisotropic (angle-dependent in the k-space) or even nodal order parameter [14]. In contrast, the $s^{\pm}$ model is based on pairing via spin fluctuations. Superconductivity is driven by the interband interaction, whereby the wave functions of the two condensates are in antiphase, which formally leads to $\Delta_L \Delta_S < 0$, where Δ_L is the large gap and Δ_S is the small gap. Because the interband interaction matrix element is negative, $V_{LS} < 0$, the magnon exchange causes attraction. Nesting between the hole and electron Fermi surface sheets causes magnetic resonance (a peak of the dynamic spin susceptibility at the nesting vector and a certain energy) [15, 16].

The model describing the formation of so-called spin and charge superstripes (nanoscale phase separation) predicts a dramatic increase in T_c caused by a Feshbach-type resonance when the Fermi level approaches the band edge (Lifshitz transition). Moreover, in this approach, the Cooper-pair condensate should be considered in an intermediate regime, between the Bardeen–Cooper–Schrieffer (BCS) condensation with significant pair overlapping (typical for classical isotropic superconductors) and the Bose–Einstein condensation, with pairs barely overlapping [9]. This approach seems reasonable for iron-based superconductors, where the semiclassical approximation $\hbar\omega_D \gg 2\Delta$ (ω_D is the Debye frequency) is inapplicable, and the average size of Cooper pairs is close to the overlapping distance.

Possible observations of flat bands in the 1111 family reported in angle-resolved photoemission spectroscopy (ARPES) measurements [17] correspond to the presence of extended van Hove singularities typical of quasi-two-dimensional compounds. In this case, the theory of cuprates by Abrikosov [18] can be used to explain the high T_c and Δ values as high as ~ 13 meV.

Each of these models suggests a certain structure of the superconducting gap and a set of some other parameters of the superconducting state. Unfortunately, despite an intensive eight-year study, the available experimental data are too contradictory to make any conclusions about the pairing mechanism. No model has unambiguous experimental confirmation yet, thus leaving the main issues unanswered. For example, the experimentally available BCS ratio $2\Delta/k_B T_c$, determined by various probes in the Ba-122 family, varies by a factor of six [19–33] (for a review, see [12, 34]). Possible reasons for this discrepancy is the strong out-of-plane gap anisotropy in the k_z space, which seems to 'smear' the gap values obtained in bulk probes, and the sensitivity of the superconducting properties to the surface quality. The gap temperature dependences measured in [28, 29] using point-contact Andreev spectroscopy (PCAR) are typical for a strong interband coupling. A number of inelastic neutron scattering probes [35–38] reported a rather sharp magnetic resonance peak, which is in favor of the $s^{\pm}$ model [15, 16]. Nonetheless, the experimentally observed intensity and line shape of the dynamic magnetic susceptibility peak does not seem so pronounced as predicted by the $s^{\pm}$ model [13, 14], and the $s^{\pm}$ pairing would be unstable in the presence of impurities [13, 39]. The absence of nesting evident from ARPES measurements [7] and the strong intraband coupling revealed from direct temperature dependences of the gaps [34, 40] support the s^{++} model. On the other hand, the proximity to the Lifshitz transition, observation of a larger gap value for the smallest Fermi surface cylinder [7, 17], nanoscale phase separation, and a Feshbach-type resonance [41, 42] indirectly support the superstripe model.

This brief review shows that reliable experimental data are essential in order to reveal the pairing symmetry and further to find a way to increase the critical temperature. Here, we present a synthesis, characterization, and comprehensive study of Ba-122 single crystals with various substitutions and T_c. Using five complementary techniques, we study superconducting properties of Ba-122 compounds and obtain a set of self-consistent data.

2. Synthesis and characterization

$BaFe_{2-x}Ni_xAs_2$ single crystals with various Ni doping levels and the critical temperature up to $T_c = 20$ K have been synthesized using the self-flux technique. To prevent oxidation in the open air, all the reagents were weighed in a glove box with a controlled argon atmosphere. Metallic Ba and high-purity FeAs and NiAs precursors, preliminarily obtained from the elements by solid-phase synthesis, were mixed in a $1 : 5(2 - x) : 5x$ molar ratio, placed in an alumina crucible, and sealed in a quartz tube under 0.2 bar of argon pressure. The ampoule was heated to 1200 °C and kept for 12 hours, triggering the reaction

$$\mathrm{Ba} + (2 - x)\,\mathrm{FeAs} + x\mathrm{NiAs} = \mathrm{BaFe_{2-x}Ni_xAs_2}\,.$$

The long exposure time is necessary in order to complete the reaction with the development of the essential phase and to make a homogeneous flux, because the doping phase $BaNi_2As_2$ diffusion into the main phase $BaFe_2As_2$ occurs via convection and is limited by the viscosity of the medium. After the exposure, the ampoule was cooled to 1150 °C, with further flux crystallization in the temperature gradient under cooling to 1050 °C at the rate of 2 °C per hour. Upon reaching the latter temperature, the liquid flux was decanted by turning over the ampoule.

The grown crystals were up to $4 \times 2 \times 0.2$ mm^3 in size. Figure 1a shows X-ray diffraction spectra of $BaFe_{2-x}Ni_xAs_2$ single crystals with $x = 0.09$ (lower curve) and $x = 0.1$ (upper curve) obtained using a DRON-2.0 diffractometer with a curved graphite monochromator. The spectra show only intensive peaks attributed to the 122 phase, thus demonstrating the high purity of the synthesized single crystals. To detect twinning boundaries or disorientation of blocks in the single crystal, we measured the rocking curves and two-dimensional (2D) plots in the vicinity of the (006) peak using the Panalytical X'Pert Pro MRD Extended diffractometer. A part of the XRD spectrum in the 2D vicinity of the (006) peak is detailed in the inset of Fig. 1a. The presence of a single peak

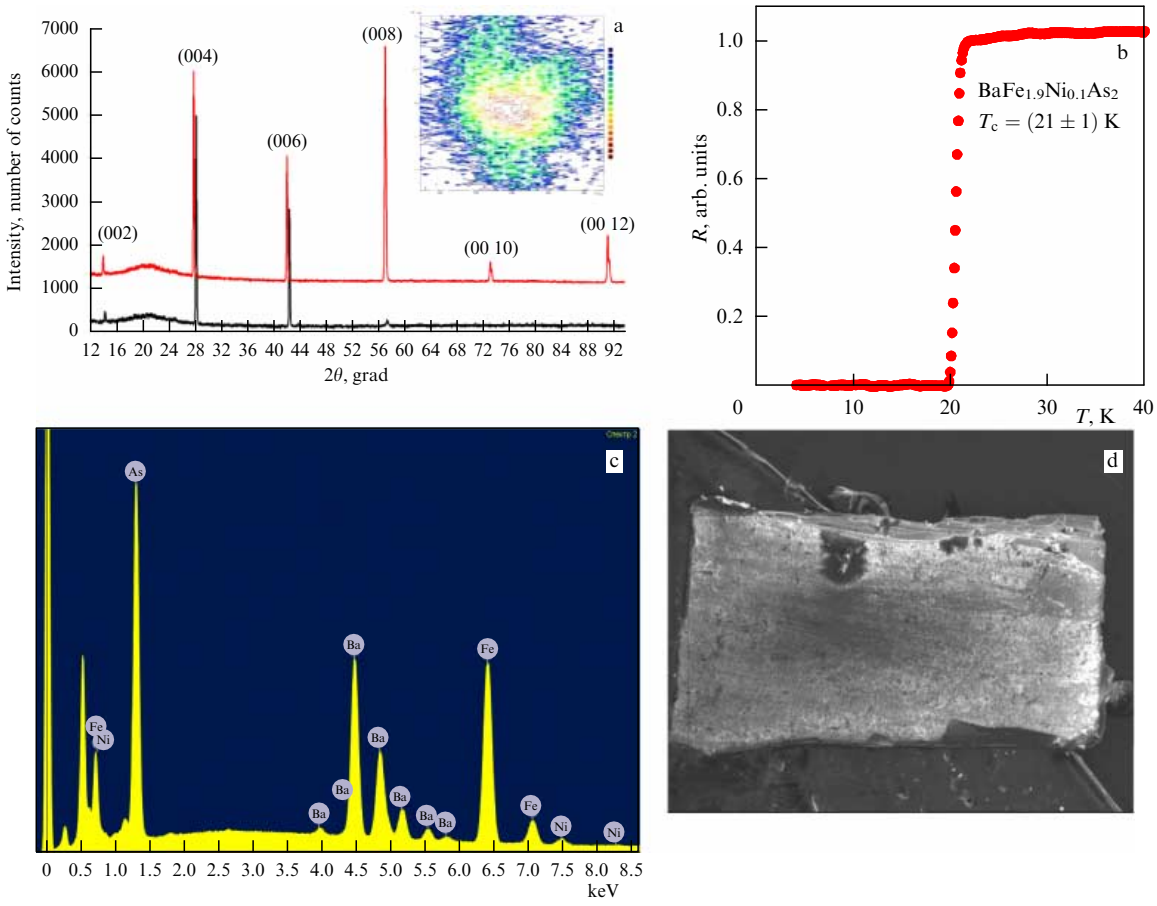

Figure 1. (a) X-ray diffraction spectra for $BaFe_{2-x}Ni_xAs_2$ single crystals with $x = 0.09$ (lower curve) and $x = 0.1$ (upper curve). The inset shows a 2D plot in the vicinity of the (006) peak. (b) Temperature dependence of resistance near the superconducting transition. (c) Energy dispersive spectrum (EDS) of a $BaFe_{1.92}Ni_{0.08}As_2$ single crystal. (d) Electron microscope image of a $BaFe_{1.92}Ni_{0.08}As_2$ single crystal with dimensions 1.5×0.8 mm^2.

in the vicinity of the (006) reflex evidences the absence of disoriented blocks in the crystal. The single high-intensity peaks (Fig. 1a) evidence the high quality of the samples and the homogeneous Ni distribution within the bulk of the crystal. Energy dispersive spectroscopy (EDS) analysis showed the elemental ratio Ba : Fe : Ni : As to be 1.06 : 1.91 : 0.09 : 1.95 (Fig. 1c), agreeing well with the nominal ratio. An electron microscope image of a $BaFe_{1.92}Ni_{0.08}As_2$ single crystal with dimensions 1.5×0.8 mm^2 is shown in Fig. 1d.

3. Study of high-field magnetization

The irreversible magnetization $M(H, T)$ was measured using a vibrating sample magnetometer and the magnetic susceptibility $\chi'(H, T)$ using a PPMS-9 susceptometer (Quantum Design) in fields up to 9 T applied along the crystal c axis. The typical field sweep rate was 100 Oe s^{-1}. The susceptibility temperature dependences (Fig. 2a) show a clear and sharp superconducting transition, pointing to the presence of a single superconducting phase with the critical temperature $T_c \approx 19$ K of the $BaFe_{1.92}Ni_{0.08}As_2$ single crystal. With the Ni concentration increase, T_c decreases. For an overdoped crystal with $x = 0.18$ and $T_c \approx 9.3$ K, the corresponding magnetic susceptibility transitions in various fields are shown in Fig. 2b. The superconducting transition width $\Delta T_c \approx 1.4$ K obtained using the susceptibility (Fig. 2b) and resistance (Fig. 1b) temperature dependence demonstrates structural perfection and homogeneity of the superconducting properties within the bulk.

Using magnetic hysteresis loop measurements, we plot the field dependence of the critical current density J_c for underdoped $BaFe_{1.92}Ni_{0.08}As_2$ (Fig. 2c) at various temperatures, which is similar to that for samples with a nearly optimal composition. The linear behavior in regime I (up to 100–150 Oe at helium temperatures) is generally attributed to the single-vortex pinning mode. At higher fields up to 0.5 T, a power-law dependence $J_c \sim H^{-\alpha}$ is observed; hence, regime II corresponds to a significant increase in the number of vortices in the bulk and their interactions. The obtained exponent is $0.37 < \alpha < 0.43$, thus being slightly lower than $\alpha = 5/8$ predicted theoretically for strong pinning centers. The observed discrepancy may point to the presence of some extended defects and scattered weak pinning centers [43]. The presence of regime III with $J_c(H) \sim$ const seems to be caused by coexisting large and small pinning centers, acting like a cage for the magnetic vortices. Strong vortex pinning is destroyed in regime IV, which is accompanied by decreasing J_c and melting of the vortex lattice. Figure 2d shows the normalized pinning force $f_p = F_p/F_{pmax}$ as a function of the normalized field $h = H/H_{irr}$ measured at various temperatures. The value of the irreversible field H_{irr} was determined as that corresponding to the critical current density turning to zero ($J_c \to 0$). Obviously, the $f_p(h, T)$ curves merge at the field $H||c$. Using the Dew–Hughes model [44] with

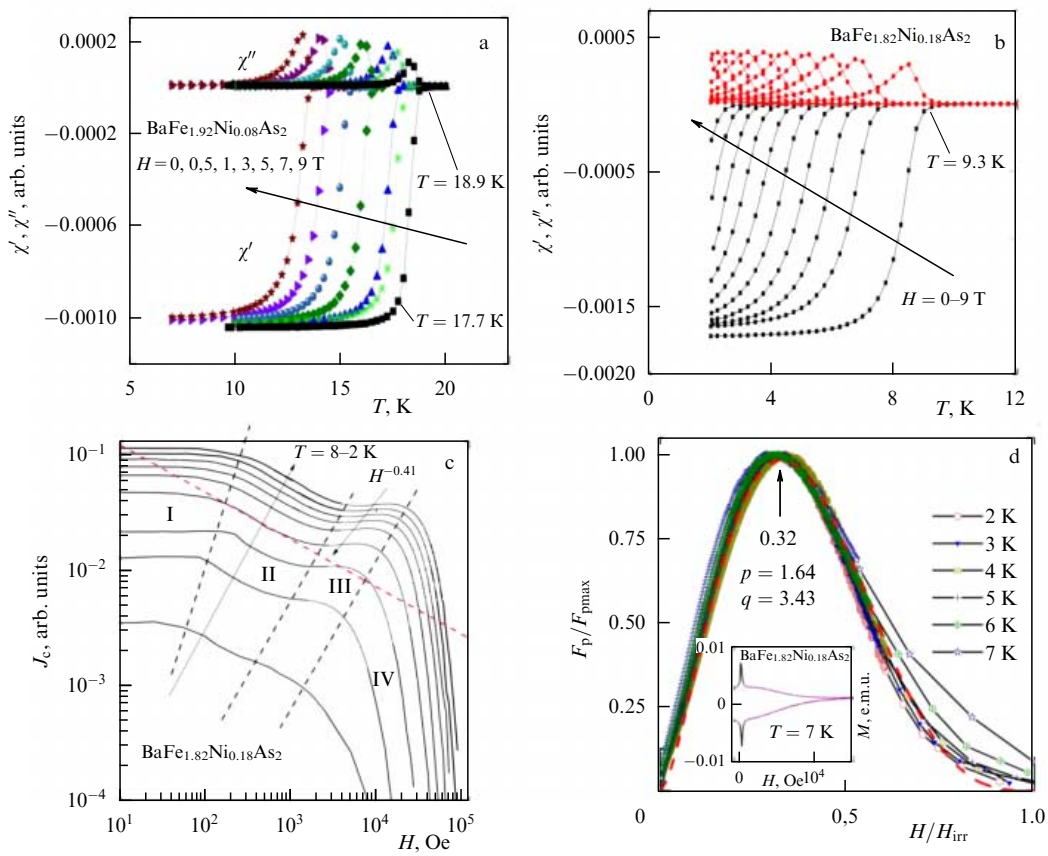

Figure 2. Temperature dependence of the magnetic susceptibility in various magnetic fields up to 9 T (a) for a slightly underdoped $BaFe_{1.92}Ni_{0.08}As_2$ single crystal, and (b) in overdoped $BaFe_{1.82}Ni_{0.18}As_2$ with $T_c \approx 9.3$ K. (c) Critical current density J_c as a function of the magnetic field H; data are taken from [40]. (d) Normalized pinning force $f_p = F_p/F_{pmax}$ as a function of the normalized field $h = H/H_{irr}$ measured at various temperatures. The inset shows the hysteretic loop at $T = 7$ K.

$f_p(h, T) \sim h^p(1-h)^q$, we obtain the exponents $p = 1.64$ and $q = 3.43$ for the $BaFe_{1.92}Ni_{0.08}As_2$ single crystal. In accordance with this model, the obtained peak $h^p = 0.32$ points to a prevalence of strong point pinning centers. Other evidence of strong bulk pinning is the high symmetry of the magnetization loop at temperatures close to T_c, which also indicates an insignificant number of magnetic impurities in the single crystal (see the inset of Fig. 2d).

4. Specific heat measurements

The specific heat was measured using the thermal relaxation technique with PPMS-9 (Quantum Design) in the temperature range 2–200 K. For the analysis of experimental data, the key, albeit most time-consuming, issue is to separate the electron part containing information about superconducting properties and the lattice part of the specific heat. The reason is that the lattice part cannot be measured directly. To overcome this, the so-called approximation of corresponding states [45] can be used. This approximation is based on using the lattice part of specific heat for a compound with a similar composition but undergoing neither a superconducting nor a magnetic transition. In the case of the Ba-122 family, we take the parent compound $BaFe_2As_2$ with a certain substitution and doping (although the parent compound undergoes a magnetic transition at 140 K). When varying the dopant or its concentration, the lattice parameters change by a few percent. To take this minor variation into account, we use scaling coefficients close to unity. As an example of such nonsuperconducting and nonmagnetic compounds similar to $Ba_{0.67}K_{0.33}Fe_2As_2$, one can choose $Ba(Fe_{0.847}Co_{0.153})_2As_2$ [46], $Ba(Fe_{0.88}Mn_{0.12})_2As_2$ [47], and $BaFe_{1.75}Ni_{0.25}As_2$ [48].

Mathematically, the corresponding state approximation can be expressed as:

$$C_{tot}^{SC}(T) = C_{exp}(T) = C_e^{SC}(T) + AC_{lat}^{nSC}(BT)\,,$$

where $C_{tot}^{SC}(T)$ is the total specific heat corresponding to the experimental $C_{exp}(T)$ data, $C_e^{SC}(T)$ is the electron part, $C_{lat}^{nSC}(T)$ is the lattice part for nonsuperconducting nonmagnetic compound, and A and B are scaling coefficients. Above T_c, $C_e^{SC}(T)$ could be regarded as $\gamma_n T$. The A and B coefficients are determined using the least square method and taking the entropy conservation into account:

$$\int_0^{T_c} \frac{C_e}{T}\,\mathrm{d}T = \int_0^{T_c} \gamma_n\,\mathrm{d}T.$$

The specific heat of the superconducting condensate could be calculated in the framework of the BCS model [49]; however, for 122 compounds, it is preferable to describe the electron part using the phenomenological two-band α-model [50]. This model elaborates the specific heat of a two-band superconductor as a sum of weighted partial contributions of the two condensates in each band. The fitting parameters are $\alpha_1 = 2\Delta_1/k_BT_c$, $\alpha_2 = 2\Delta_2/k_BT_c$, and the weight factor φ_1 (where $\varphi_i = \gamma_i/\gamma_n$, γ_i is the specific heat of the ith condensate in the normal state), which can be obtained using the least square method.

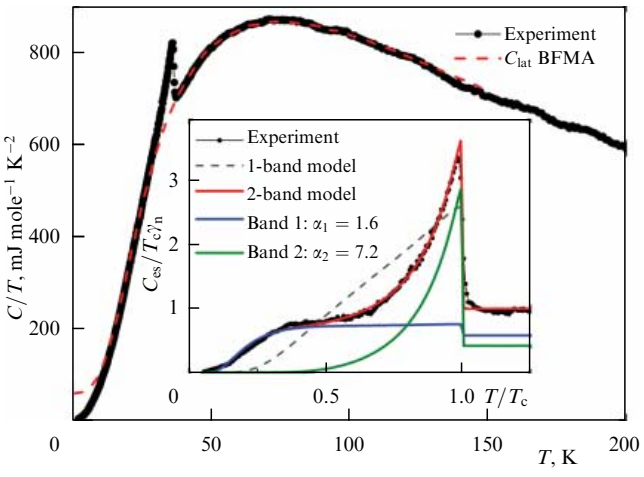

Figure 3. (Color online.) (a) Temperature dependence of the specific heat for a $Ba_{0.67}K_{0.33}Fe_2As_2$ sample, normalized by temperature in a zero field. Red dashed line is the corresponding state approximation fit using the lattice specific heat of $Ba(Fe_{0.88}Mn_{0.12})_2As$ (BFMA). The inset shows the normalized electron part of the specific heat of the superconducting condensate $C_{es}/T\gamma_n$ fitted using the single-band model (dashed line) and the two-band BCS α-model (solid curves). The data are taken from [51].

The specific heat measurements were made with a 1.93 mg piece of a $Ba_{1-x}K_xFe_2As_2$ ($x = 0.33$) single crystal cleft from the same large crystal that was used for all other measurements; the sample had the critical temperature $T_c = 36.5$ K. The raw experimental specific heat is shown in Fig. 3 in the zero field. At temperatures tending to zero, the $C(T)/T$ dependence could be extrapolated to zero, similarly to the Debye law $C(T)/T = \gamma(0) + \beta T^2$ [51], showing no features in the low-temperature range (such as growth towards the lowest T or a Schottky anomaly), thus evidencing the high quality of the sample.

In the temperature interval 36–37 K, the specific heat $C(T)$ demonstrates a sharp peak related to the superconducting transition (see Fig. 3). The peak width is about 1 K, and the jump in the C/T data at the transition is $\Delta C/T = 119$ mJ mol^{-1} K^{-2}. To separate the lattice and electron parts, we used the specific heat of the reference compound $Ba(Fe_{0.88}Mn_{0.12})_2As_2$ [31], because the specific heat data for that compound was measured within the widest temperature range. Figure 3a shows that the corresponding state approximation provides good agreement between the experimental data and the data obtained with the modified lattice specific heat of $Ba(Fe_{0.88}Mn_{0.12})_2As_2$. The resulting normalized electron part of the superconducting condensate $C_{es}/T\gamma_n$ (see [51] for details) fitted with various theoretical models is shown in the inset in Fig. 3. The single-band approach with an isotropic order parameter gives an optimum result for $2\Delta/k_BT_c = 3.7$. Nonetheless, this approach is obviously insufficient to describe the superconducting properties of Ba-122: the corresponding theoretical $C(T)$ curve (the dashed line in the inset in Fig. 3) does not fit the remarkable hump in $C_{es}/T\gamma_n$ clearly seen at $T/T_c \sim 0.3-0.5$. On the other hand, the phenomenological two-band approach (α-model, the red line in the inset in Fig. 3) reproduces the data well. The difference between the model dependence and the experimental data does not exceed 5% of $C_{es}/T\gamma_n$, which corresponds to 4 mJ mol^{-1} K^{-2}. The deviation is within the measurement uncertainty and in relative units does not exceed 1% of the total measured C_{exp}. With the two-band model, we find the following set of parameters: $\alpha_1 = 2\Delta_1/k_BT_c = 1.6 \pm 0.1$ ($\Delta_1 = (2.5 \pm 0.2)$ meV), $\alpha_2 = 2\Delta_2/k_BT_c = 7.2 \pm 0.2$ ($\Delta_2 = (11.3 \pm 0.3)$ meV), and $\varphi_1 = 0.58 \pm 0.02$.

5. Optical spectroscopy

Optical spectroscopy is one of the basic techniques to explore electrodynamic properties of superconductors [52, 53]. The penetration depth is of the order of several hundred nanometers, which facilitates bulk probes, in particular, measurements of superconducting gaps.

In the case of a single-band superconductor with an isotropic gap, electromagnetic radiation with the energy less than the superconducting gap value 2Δ cannot be absorbed by the sample. This leads to the vanishing of the real part of the complex optical conductivity σ at $T \ll T_c$ and at a frequency lower than that corresponding to the doubled superconducting gap 2Δ; the reflectance, in its turn, tends to unity. As a result, the optical response shows a feature at a frequency in the vicinity of 2Δ. In particular, for a bulk single crystal, a peak in the spectrum of the relative reflectance $R(T)/R(T > T_c)$ must be observed.

Because the $Ba_{1-x}K_xFe_2As_2$ ($x = 0.33$) sample was not large enough for accurate measurements of the absolute value of reflectance [51], we used the technique described in [54] to determine the superconducting gaps. This technique is based on the measurement of the relative reflectance $R(T)/R(T > T_c)$ and enables minimizing possible temperature-driven distortions of the optical setup, which may yield frequency-dependent systematic errors in $R(\omega)$. We note that for bulk s-wave superconductors, the normalized reflectance $R(T \ll T_c)/R_N$ (where R_N is the reflectance in the normal state just above T_c) has a maximum corresponding to 2Δ. For two-gap superconductors, the maximum is expected between the two SC gaps, closer to the one making the major contribution. Infrared-range measurements were done using a Bruker Optics IFS-125HR Fourier-transform IR spectrometer.

Figure 4 shows the normalized $R(T)/R(T = 40\text{ K})$ dependences measured at $T = 5-50$ K. We can see that the normalized reflectance $R(T)/R(40\text{ K})$ starts increasing as the temperature T decreases below T_c. This is because the reflectance approaches unity at energies $\hbar\omega < 2\Delta$ for s-wave superconductors at temperatures below T_c. Hence, the peak

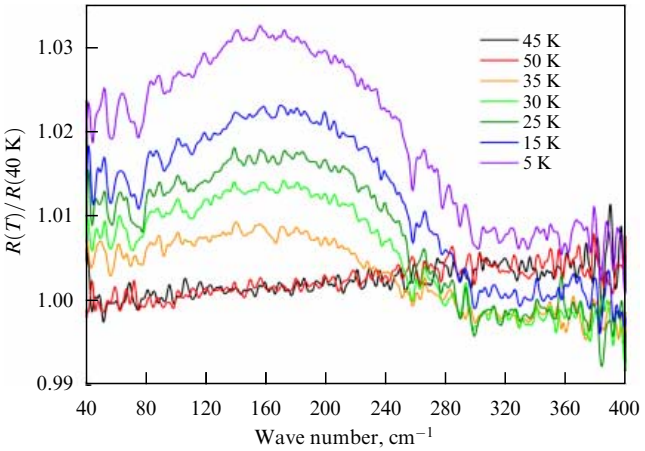

Figure 4. Normalized reflectivity $R(T)/R(40\text{ K})$ of $Ba_{0.67}K_{0.33}Fe_2As_2$ measured at $T = 5-50$ K. The data are taken from [51].

at ≈ 160 cm^{-1} (19.8 meV) can be used as an estimate for the magnitude of the larger superconducting gap $\Delta_L \approx 10$ meV [25–27, 47]. The smaller gap is beyond the frequency range of our IR measurements. The kink in the normalized reflectance at ~ 250 cm^{-1} is probably caused by the IR active phonon mode E_u related to Fe(ab)–As($-ab$) vibrations [55]. This mode manifests itself in many AFe$_2$As$_2$ materials, including A = Ca, Sr, Eu, and Ba.

6. Intrinsic multiple Andreev reflection effect (IMARE) spectroscopy

Multiple Andreev reflections effect (MARE) spectroscopy is a unique direct probe of the bulk superconducting order parameter [56–58]. MARE occurs in a ballistic [59] superconductor–normal-metal–superconductor (SnS) junction whose size $2a$ is less than the carrier mean free path l. MARE causes a pronounced excess current at low bias voltages (so-called 'foot') and a subharmonic gap structure (SGS). In a high-transparency SnS junction (of the order of 95–98%), the SGS is a series of dynamic conductance dips at bias voltages $V_n = 2\Delta/en$, where Δ is the superconducting gap, e is the elementary charge, and $n = 1, 2, \ldots$ is the subharmonic order [60–63]. Probing the SnS junction is a unique opportunity to directly determine the gap value using the positions of Andreev subharmonics for temperatures $0 < T < T_c$ (as shown theoretically in [60, 63]), enabling direct measurement of the temperature dependences of the gaps and providing a local critical temperature (with T_c corresponding to the contact area transition to a normal state). The value of T_c^{local} is essential for an accurate estimation of the most important superconducting parameter, the BCS ratio $2\Delta/k_B T_c$. Evidently, in a two-gap superconductor, two distinct gaps would cause two SGSs in the $dI(V)/dV$ spectrum.

The angle dependence of the superconducting gap in k-space strongly affects the shape of Andreev features [58, 64, 65]. The isotropic (fully s-wave) gap produces sharp high-intensive and symmetric dynamic conductance dips, whereas a d-wave or fully anisotropic s-wave gap (with nodes at some angles in k-space) make the subharmonics poorly visible and strongly asymmetric. An anisotropic gap with a cos (4θ)-type angular distribution in the $k_x k_y$ plane of the momentum space (which is very likely the case for Ba-122 [14,15]) causes doublet-like features in the $dI(V)/dV$ spectrum of a tunneling contact for c-direction transport [66]. The doublet represents two minima connected by an arch, whose positions correspond to the upper and lower extremes of the cos (4θ)-type gap angular distribution [58].

In Ba-122, high-quality SnS contacts were formed by the 'break-junction' technique [58, 67]. A single crystal prepared as a thin rectangular plate was attached to a springy sample holder (oriented along the ab plane) using four pads of In–Ga paste and then cooled to $T = 4.2$ K. In the liquid He environment, a gentle mechanical curving of the sample holder produced a cleavage of the sample, thus creating two superconducting banks separated with a weak link. As a result, an ScS contact was formed, where 'c' denotes a weak link (constriction). Judging by the resulting current–voltage characteristics (CVCs) of the contacts made in Ba-122 [62], the constriction formally acts as a thin layer of normal metal. The relation between the contact diameter and the carrier mean free path indicates that the break junctions are in the ballistic regime, thus making it possible to observe MARE [40, 60–63, 68]. In the configuration we employed, the superconducting banks are not separated but slide along each other in the ab plane; therefore, the cryogenic clefts remain clean and do not degrade during the experiment. Our technique facilitates probing several dozen ScS contacts with various dimensions, resistances, and transparencies. We have collected a large amount of data with each sample in order to check the data reproducibility and exclude the influence of spatial effects.

Another unique feature intrinsic to the break-junction technique is the formation of natural ScSc...S arrays [40, 51, 56–58, 68] in layered superconducting materials. These usually exfoliate along the ab planes with the formation of steps and terraces along the c-direction, where an intrinsic multiple Andreev reflection effect (IMARE) occurs. The IMARE resembles the intrinsic Josephson effect [69] and was first observed in cuprates, and later in other layered superconductors (see [58] for a review). When considering an Andreev array as a sequence of m identical SnS junctions, the bias voltage of the SGS scales with m as $V_n = 2\Delta m/en$, where $n, m = 1, 2, \ldots$. In order to determine m and the value of the gap(s), we must find natural numbers that scale the $I(V)$ and $dI(V)/dV$ curves for various arrays onto each other or achieve the position of gap features coincident with those for a single-junction spectrum. In an array, just as in a natural structure of the crystal, a contribution of bulk effects well exceeds that of the surface influence [40, 57, 58]. Strictly speaking, IMARE spectroscopy is currently the only technique probing the bulk values of superconducting gap(s) locally (within the contact area of 10–50 nm) [58]. The experimental setup is detailed in [58, 70].

Figure 5 shows a CVC with an excess current and a pronounced foot area at low bias voltages, which are typical for the high-transparency SnS regime. The dynamic conductance spectra (data from [68]) correspond to the two SnS

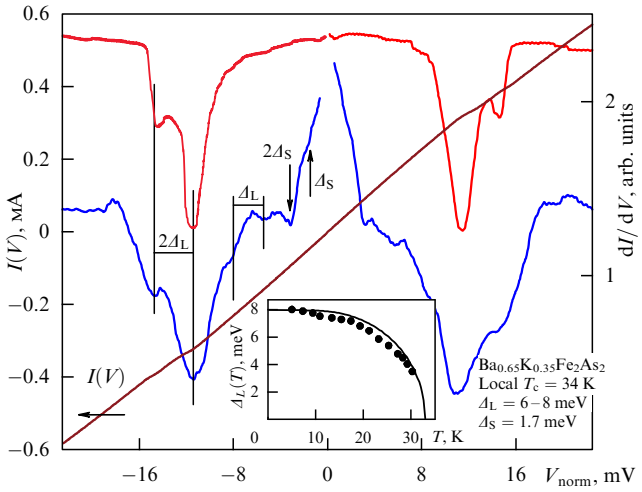

Figure 5. Current–voltage characteristic $I(V)$ (left vertical scale) and the dynamic conductance spectrum (right scale) for SnS Andreev contacts with the local critical temperature $T_c = 34$ K measured in a $Ba_{0.65}K_{0.35}Fe_2As_2$ single crystal at $T = 4.2$ K. The doublet minima of the anisotropic large gap $\Delta_L = 6-8$ meV (the range corresponds to the angle-dependent magnitude distribution in the k-space) and subharmonics of the small gap $\Delta_S \approx 1.7$ meV are marked with respective vertical black bars and arrows. The inset shows the large gap temperature dependence (dots) and single-band BCS-like behavior for comparison. The data are taken from [51, 68].

arrays obtained with $Ba_{0.65}K_{0.35}Fe_2As_2$ single crystals from the same batch (the synthesis and characterization are detailed in [71, 72]). The local critical temperature of these contacts is $T_C^{local} = 34$ K. The dynamic conductance spectra have clear and well-reproduced doublet features at bias voltages corresponding to the doubled large gap $2\Delta_L \approx 12-16$ meV. The lower spectrum also demonstrates the second subharmonic of the large gap at $V \approx \Delta_L/e \approx \pm(6-8)$ meV, where the range corresponds to the doublet edges. The width of the dynamic conductance doublets probably reflects the in-plane anisotropy of the large gap in the momentum space. On the other hand, the external minima (whose position corresponds to the upper gap edge) are less pronounced than the internal ones. This seems to result from the angular distribution of the gap in k-space being more complex than $\Delta_L(\theta) \sim 0.5[1 + A\cos(4\theta)]$, $A < 1$. The small-gap SGS is resolved in the lower spectrum: the first subharmonic is at $V_1 \approx \pm 3.4$ mV and the second at $V_2 \approx \pm 1.7$ mV. A possible anisotropy of the small gap is a problem for further studies. A possible anisotropy of the small gap should be probed in further studies. Using the expression for the SGS, it is easy to obtain the two gaps: $\Delta_L \approx 6-8$ meV ($\sim 25\%$ in-plane anisotropy) and $\Delta_S \approx 1.7$ meV. The inset shows the temperature dependence of the upper extremum of the large gap.

In nearly optimal Ni-substituted $BaFe_{2-x}Ni_xAs_2$ crystals [40], we resolved a similar in-plane anisotropy of the large gap. In Fig. 6, we compare the normalized $dI(V)/dV$ spectra for two SnS arrays with various numbers of junctions formed by a sequential mechanical readjustment in the same sample [40]. The spectra look quite similar, and hence these contacts seem to be obtained in the same area of the cryogenic cleft. During a precise change in the holder curvature, the touching point of the two cryogenic clefts seemed to jump to a neighboring terrace, thus changing the number of acting layers (the number of contacts in the stack) from $m = 10$ (upper spectrum) to $m = 9$ (lower spectrum). In Fig. 6, the bias voltages of these curves were divided by the corresponding integer m; after the normalization, the positions of the main dynamic conductance features coincide. The inset in Fig. 6 shows $I(V)$ curves for these SnS arrays. A pronounced excess current near zero bias is typical for the high-transparency Andreev regime. The contact resistance is large enough to provide ballistic transport [59], allowing the IMARE to be observed. Black vertical bars show the $n = 1$ and $n = 2$ doublet SGS features for the large gap. We note that the $n = 2$ doublet located at $V_2 \approx \pm(3.2-4.4)$ mV is half as wide as the first one at $V_1 \approx \pm(6.4-8.8)$ mV corresponding to $2\Delta_L$, which is in good agreement with the SGS formula. Therefore, the large gap is $\Delta_L \approx 3.2-4.4$ meV and has a $\sim 30\%$ in-plane anisotropy, similar to that in the BKFA cited above [68]. The arrows in Fig. 6 point to the main ($n = 1$) subharmonics for the small gap. These dips are much more intensive than those of the large gap, and do not match the expected position of the third subharmonic for Δ_L (expected at $V_3 \approx \pm(2.2-2.9)$ mV, according to the SGS formula). These doublets, although slightly overlapping the V_2 position, determine the small gap $\Delta_S \approx 1.6$ meV.

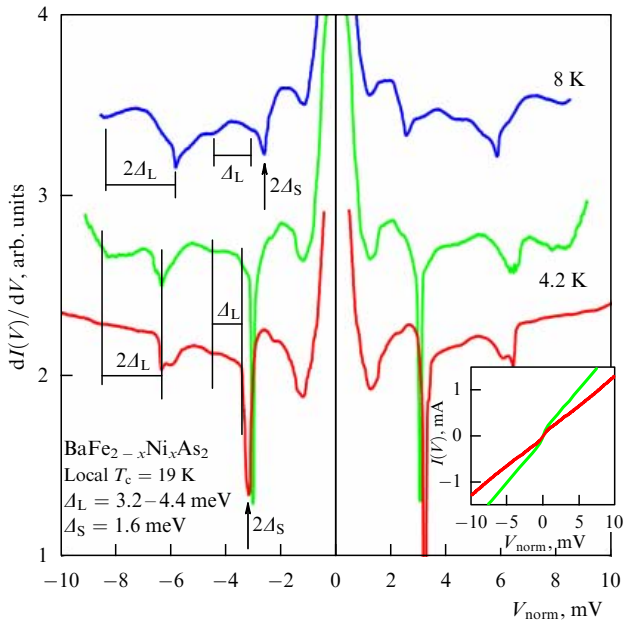

Figure 6. (Color online.) Normalized dynamic conductance spectra for SnS arrays with the local critical temperature $T_c = 19$ K (the lower $dI(V)/dV$ spectrum corresponds to $m = 10$ junctions in the array, the upper spectra $dI(V)/dV$ to $m = 9$ measured at $T = 4.2$ and 8 K) for a $BaFe_{1.9}Ni_{0.1}As_2$ single crystal. The doublet minima of the anisotropic large gap $\Delta_L(4.2\text{ K}) = 3.2-4.4$ meV and the small gap $\Delta_S(4.2\text{ K}) = 1.6$ meV are shown with vertical bars and arrows. The inset shows the current–voltage characteristics of these contacts at $T = 4.2$ K. The data are taken from [40].

To show unambiguously that the features indicated by the arrows correspond to a distinct SGS unrelated to Δ_L, it is reasonable to probe the temperature influence on the spectrum. For the junction whose spectrum is shown with a light green curve, $T \approx 4.2$ K, evolution of the spectrum at $T \approx 8$ K is shown with the upper curve. Obviously, the features shown by arrows significantly shift toward zero, accompanied by a dramatic reduction in their intensity with an increase in T by a factor of two. By contrast, this is not the case with Δ_L subharmonics. We note that the dips at $V \approx \pm 1.2$ mV observed in both spectra do not correspond to the second subharmonic of the small gap and could be attributed to the onset of the foot area at low biases.

Measurements of the dynamic conductance spectra in the temperature range from 4.2 K to T_c enable directly obtaining the temperature dependence of the gaps shown in Fig. 7. It is noteworthy that the doublet structure of the Δ_L subharmonics is well resolved up to T_c, keeping a nearly constant $33 \pm 3\%$ anisotropy (see Fig. 7b). The temperature dependences of the outer and inner extremes of Δ_L are similar: $\Delta_L(T)$ lies somewhat lower than the single-gap BCS-like dependence (the dashed-dotted line in Fig. 7). By contrast, the small-gap behaviors differ: $\Delta_S(T)$ is bent down; this is typical for an induced superconductivity within a wide range of temperatures caused by a proximity effect in the k-space. Nonetheless, this feature of $\Delta_S(T)$ is not a result of the superconducting bulk order parameter Δ_L induced onto the cleft surface: the temperature dependence determined from the spectra of SnS arrays barely delivers the bulk properties of the material. The difference between the $\Delta_L(T)$ and $\Delta_S(T)$ temperature behavior therefore indicates that the corresponding $dI(V)/dV$ features relate to two distinct superconducting condensates.

Remarkably, the experimental $\Delta_{L,S}(T)$ dependence could be fitted with a two-band model based on the Moskalenko and Suhl system of equations with a renormalized BCS integral [73, 74]. This system of equations determines the shape of gap temperature dependences using a set of electron–boson coupling constants $\lambda_{ij} = V_{ij}N_j$, where $i, j = L, S$

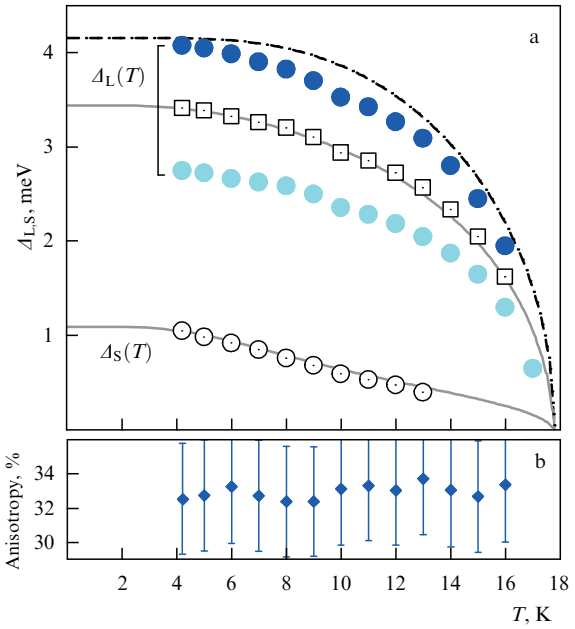

Figure 7. (a) Temperature dependences of the outer and inner extremes of the large gap (solid dots), and the outer extreme of the small gap (circles) for $BaFe_{1.9}Ni_{0.1}As_2$. Squares depict the temperature dependence of the average Δ_L value. A BCS-like curve for Δ_L^{max} is shown by the dashed-dotted line. Solid lines correspond to theoretical fits of $\Delta_{L,S}(T)$ using the two-band model based on the Moskalenko and Suhl gap equations. (b) The temperature variation of the large gap anisotropy taken as $1 - \Delta_L^{min}/\Delta_L^{max}$.

(hereafter, the index S relates to the effective band with the small gap, and the index L to that with the large gap), V_{ij} are interaction matrix elements, and N_j is the normal density of states at the Fermi level. We take the average $\Delta_L(T)$ as a 'driving' gap value; its temperature dependence is shown in Fig. 7 by squares. To fit the experimental data numerically using the BCS-like two-band model, we take the Debye energy $\hbar\omega_D = 20$ meV [75] and use the following fitting parameters: the ratio between the densities of states in the two bands N_S/N_L and the intra-to-interband interaction ratio. The fitting with this model is detailed in [76, 77]. We only note that the fitting cannot reveal the sign of interband constants $\lambda_{i\neq j}$; thus, the four constants obtained are not full λ_{ij}^{Full} (involving a Coulomb interaction μ^*), but the effective $\lambda_{ij} = \lambda_{ij}^{Full} - \mu_{ij}^*$.

The calculated theoretical curves $\Delta_{L,S}(T)$ (solid lines in Fig. 7) are typical for a strong intraband and a moderate interband interaction. The deviation of the $\Delta_L(T)$ dependence from a single-band BCS-like curve seems to result from th influence of the 'weak' band having the larger density of states at the Fermi level. Due to the nonzero interband coupling, both gaps vanish at the same critical temperature T_c^{local}.

Despite the complex structure of the order parameter in Ba-122, the experimentally observed temperature dependence of the gaps agrees qualitatively with that predicted by the simple two-band model. This allows using the estimated parameters to make some important conclusions concerning the superconducting state features of Ba-122. First of all, the 'eigen' superconductivity (in the hypothetical case of a zero interband interaction $V_{LS} = 0$) of the bands with a small gap tends to that described by the weak-coupling BCS limit: in accordance with our estimations, the characteristic ratio $2\Delta_S/k_B T_c^S \approx 3.5$ (where T_c^S is the 'eigen' critical temperature of the Δ_S-condensate at $V_{LS} = 0$). The set of estimated absolute values $\lambda_{LL} \approx 0.37$, $\lambda_{SS} \approx 0.23$, $|\lambda_{LS}| \approx 0.07$, and $|\lambda_{SL}| \approx 0.02$, under the assumption of zero Coulomb repulsion, $\mu^* = 0$, typical for $s^{\pm}$-models [15, 16], leads to the extremely high density-of-states ratio $N_S/N_L \approx 3.5$ and a tiny interband coupling with $\sqrt{V_L V_S}/V_{LS} \approx 7.3$; this result contradicts the idea of the $s^{\pm}$-pairing. On the other hand, assuming a moderate Coulomb repulsion $\mu_{ij}^* \approx 0.13$, we obtain the following set of full constants: $\lambda_{LL} \approx 0.50$, $\lambda_{SS} \approx 0.36$, $|\lambda_{LS}| \approx 0.2$, and $|\lambda_{SL}| \approx 0.15$. In this case, the density of states in the 'weak' effective band is only 1.5 times larger than N_L of the 'driving' band, in accordance with the band-structure calculations [78], and the intraband coupling is 2.7 times stronger than the interband one. It follows that the moderate Coulomb repulsion is essential in order to describe the superconducting properties of iron-based pnictides.

7. Measurements of the lower critical field

The lower critical field measurement technique using magnetization curves is based on the determination of the field where the $M(H)$ dependence starts deviating from the linear $M(H) \sim H$ behavior corresponding to vortex penetration into the bulk of the sample. Our magnetization measurements were performed using the MPMS-XL7 (Quantum Design) SQUID magnetometer.

In the vicinity of H_{c1}, the magnetization curve can be written as

$$M(H) = \begin{cases} aH + b\,, & H < H^* \\ aH + b + c(H - H^*)^2\,, & H > H^*\,. \end{cases}$$

For all the H^* points at which magnetization was measured, we chose the a, b, and c parameters to fit the experimental data (b corresponds to a negligible deviation of the magnetization in the zero field from zero). We then calculate the correlation index, which demonstrates a clear maximum in the dependence on H^*; the maximum is located at H_{c1}.

In $Ba_{1-x}K_xFe_2As_2$, the London penetration depth λ ($\sim 100-200$ nm) is much larger than the coherence length ξ ($\sim (2-2.5)$ nm) (see [79] for details), and therefore a local London model is applicable to this compound. The normalized superconducting density is then given by

$$\bar{\rho}_S^0(T) = \frac{\lambda_{ab}^2(0)}{\lambda_{ab}^2(T)} \approx \frac{H_{c1}(T)}{H_{c1}(0)}\,.$$

The resulting temperature dependence of the normalized superconducting density is shown in Fig. 8 [51] for a $Ba_{0.67}K_{0.33}Fe_2As_2$ single crystal with $T_c \approx 37$ K.

Furthermore, for a single-band superconductor [80],

$$\bar{\rho}_S^0(T) = 1 + 2\int_{\Delta(T)}^{\infty} \frac{\partial f}{\partial E} \frac{E\,dE}{\sqrt{E^2 - \Delta^2(T)}}\,,$$

where $f = \exp\left[E/(k_B T) + 1\right]$ is the Fermi function, $\Delta(T)$ is the BCS-like gap temperature dependence, $E^2 = \varepsilon^2 + \Delta^2(T)$, E is the total energy, and ε is the single-particle energy offsetting the Fermi level. In this model, we used $H_{c1}(0)$ and $\alpha = 2\Delta(0)/(k_B T_c)$ as fitting parameters in order to reproduce the experimental data.

Fitting of the lower critical field data in the framework of the single-band BCS-like model [80] is shown in Fig. 8.

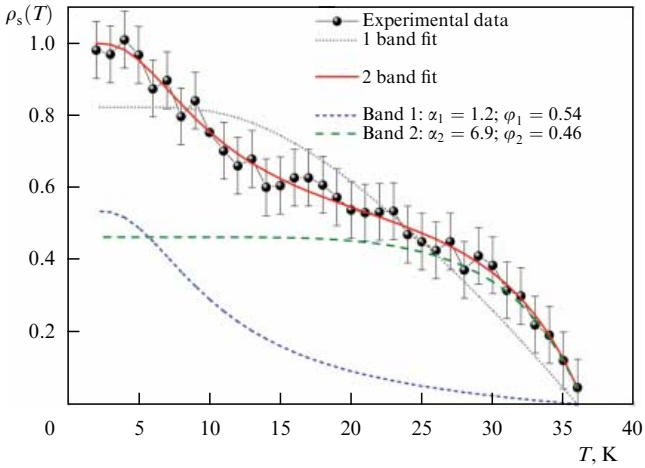

Figure 8. Temperature dependence of the normalized superconducting density for a $Ba_{0.67}K_{0.33}Fe_2As_2$ single crystal with $T_c \approx 37$ K fitted with a single-band (dotted line) and a two-band (solid line) model. Partial contributions of the bands are shown by dashed lines. The data are taken from [51].

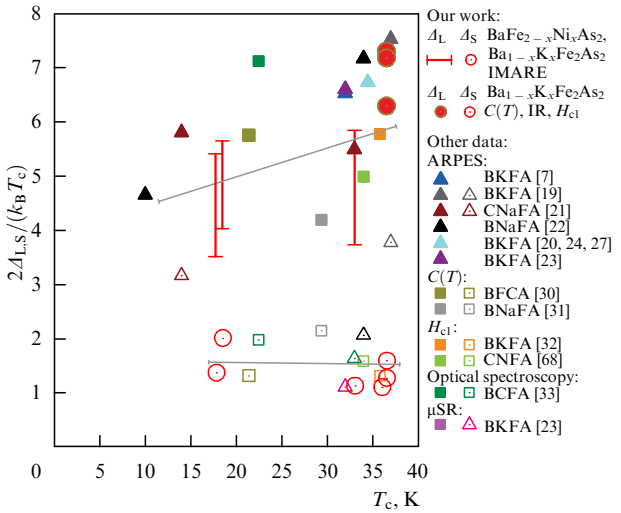

Figure 9. (Color online.) Dependence of the BCS ratio on the critical temperature for the large gap (solid symbols) and small gap (open symbols) for Ba-122 crystals with various compositions. Our data are shown by circles, and the in-plane gap anisotropy resolved in IMARE probes is shown by red vertical bars. The ARPES data [7, 19–24, 27] (triangles), and data using C(T), muon-spin-rotation, optical spectroscopy, and lower critical field measurements [30–33, 68] (squares) are shown for comparison.

Obviously, the single-band model is insufficient to describe the data. Further, we used a phenomenological two-band α-model [80, 81], where

$$\bar{\rho}_S^0(T) = \varphi\bar{\rho}_{S1}^0(T) + (1-\varphi)\,\bar{\rho}_{S2}^0(T)\,,$$

where $\bar{\rho}_{S1}^0(T)$ and $\bar{\rho}_{S2}^0(T)$ are the normalized superconducting densities for the two condensates taken with weight coefficients φ and $1-\varphi$. In this model, we vary the four fitting parameters: $\alpha_1 = 2\Delta_1(0)/(k_B T_c)$, $\alpha_2 = 2\Delta_2(0)/(k_B T_c)$, the weight contribution of one band φ, and $H_{c1}(0)$. Obviously, the two-band model reproduces the data points well (see Fig. 8). From the fit, we extract the following values: $\Delta_L(0) = (11.5 \pm 0.5)$ meV, $\Delta_S(0) = (2 \pm 0.35)$ meV $(\varphi = 0.46 \pm 0.02)$ and $2\Delta_L(0)/(k_B T_c) = 6.9 \pm 0.3$, $2\Delta_S(0)/(k_B T_c) = 1.2 \pm 0.2$. $H_{c1}(0)$ is 25.5 Oe. We note that the determined $H_{c1}(0)$ value is the lower critical field ignoring the demagnetization factor for the particular sample. However, the normalized $H_{c1}(0)$ value is used in the calculations; therefore, only the shape of the temperature dependence is essential to obtain the superconducting parameters.

8. Discussion

Undoubtedly, the experimentally determined properties of strongly anisotropic compounds (in this case, having a layered crystal structure) are sensitive to a variety of internal and external influences and to the experimental conditions. The current stage of the theoretical description of multi-gap superconductors is not yet perfect. Obviously, comprehensive studies are necessary in order to explore the complex multigap structure of the order parameter in the Ba-122 family superconductors. Comparing the results obtained by local and nonlocal, bulk, and surface techniques is essential for obtaining a reliable base for understanding the physical features of novel HTSC materials.

The data obtained in specific heat, lower critical field, and SnS Andreev spectroscopy studies revealed the presence of two distinct bulk superconducting order parameters. The large gap magnitude determined by optical probes is close to the values determined over the entire bulk as obtained in $(H_{c1}(T), C(T))$, and locally (MARE, IMARE). There is no doubt as to the bulk nature of the gaps, because the Δ_L and Δ_S magnitudes determined using single SnS contacts (MARE) and natural Andreev arrays (IMARE) of SnSn...S contacts are reproducible and independent of the contact dimension or resistance. The temperature dependences $H_{c1}(T)$, $C(T)$, and $\Delta_{L,S}(T)$ are well fitted with the two-band model. The majority of ARPES probes [19, 20, 22, 23] also confirm two gaps with different values.

Figure 9 shows a characteristic BCS ratio versus T_c for the data obtained in our studies with $Ba_{1-x}K_xFe_2As_2$ and $BaFe_{2-x}Ni_xAs_2$ compounds (red symbols) and the data from the literature, including those for 122-arsenides with other compositions. The in-plane gap anisotropy in k_xk_y-space resolved in IMARE measurements is shown by red vertical bars. ARPES (triangles) [19–24, 27], lower critical field [32, 68], specific heat [30, 31], muon-spin-rotation (μSR) [23], and optical spectroscopy [33] (squares) data are scattered substantially within the range $2\Delta_L/(k_B T_c) \approx 4.2-7.5$. The following reasons could cause this variance:

(a) local (tunneling techniques, Andreev spectroscopy, ARPES) and nonlocal (H_{c1}, $C(T)$, IR-spectroscopy) probes of the order parameter, obviously, provide different $2\Delta/(k_B T_c)$ values in the case of inhomogeneous samples;

(b) data obtained by bulk techniques are integrated over the entire sample and could be affected by a substantial energy dependence of the superconducting order parameter typical for strongly coupled superconductors; such a dependence is introduced in the framework of the Eliashberg theory. If this is the case, tunneling, Andreev, and optical probes would reveal a so-called gap edge Δ_{edge}, whereas bulk techniques give an energy-averaged gap value, which could be 'shifted' to either lower or higher values (depending on the $\mathrm{Re}\,\Delta(\omega) > \Delta_{edge}$ to $\mathrm{Re}\,\Delta(\omega) < \Delta_{edge}$ contribution ratio). In our studies, $2\Delta_L/(k_B T_c)$ determined in optical and Andreev studies are close, while those obtained using H_{c1} and $C(T)$ are somewhat higher, thus supporting the above argument;

(c) the order parameter is possibly anisotropic in both the $k_x k_y$-plane and the k_z-direction, as discussed, for example, in [14]. In particular, a nonlinear $\Delta_L(k_z)$ dependence indirectly follows from the periodic change in the Δ_L value under the energy variation of incident light in ARPES studies [20]. In this case, the bulk techniques (H_{c1}, $C(T)$) would give a gap value averaged over the k_z-direction and hence different from that obtained by surface techniques (IR spectroscopy, PCAR);

(d) a possible disparity of the surface and bulk superconducting properties, which would distort the data obtained by surface-sensitive probes;

(e) a possible nontrivial in-plane angle distribution of the gap, different from $\Delta(\theta) \sim 0.5[1 + A\cos(4\theta)]$ (where θ is an angle in the $k_x k_y$-plane, $A < 1$), widely discussed in the literature. Likewise, this could be a serious problem when interpreting the gap features.

Nonetheless, our data obtained by five experimental techniques with Ba-122 compounds are in good agreement:

(1) Our data confirm the absence of nodes in the in-plane angular distribution of the large gap in nearly optimal $(Ba, K)Fe_2As_2$ with $T_c = 34-36.5$ K, and in $Ba(Fe, Ni)_2As_2$ with $T_c \approx 18$ K;

(2) The characteristic BCS ratio $2\Delta_L/(k_B T_c) \approx 5.5-7.2$ well exceeding the BCS limit 3.5 is a consequence of strong coupling in the 'driving' bands. For the small gap, the smallness of $2\Delta_S/(k_B T_c) \approx 1.2-1.6$ results from the induced superconductivity in these bands at $T > T_c^S$, where T_c^S is the 'eigen' critical temperature of the Δ_S bands and much less than the common T_c of the compound. In bands with a small gap, despite their quasi-two-dimensionality, a weak superconductivity is developed, with an 'eigen' BCS ratio close to 3.5. Remarkably, in iron-based oxypnictides, the intraband coupling within the small gap bands is apparently somewhat stronger: according to our estimations, on average, $2\Delta_S/(k_B T_c^S) \approx 4$ [34, 77, 82]. Nonetheless, the weak superconductivity of Δ_S bands in Ba-122 is not exceptional: in magnesium diborides, 'eigen' superconductivity in the 3D π-condensate similarly tends to the BCS limit [76, 77]. We believe that a comparison of the properties of the 'weak' bands in available two-gap superconductors, such as magnesium diborides and iron-based compounds, is a challenging problem and therefore requires special theoretical studies;

(3) The BCS ratios determined in IMARE studies of (Ba, K) and (Fe, Ni) substituted single crystals in a wide range of critical temperatures are in good agreement. The anisotropy of the large gap remains nearly constant. Our data obtained by five probes show that both gaps scale linearly with T_c in the range 18–34 K: the change in the critical temperature by a factor of 1.9 for $(Ba, K)Fe_2As_2$ causes an increase in the large gap by nearly a factor of two compared with that in $Ba(Fe, Ni)_2As_2$. Although the electron doping by (Ba, K) substitution affects the structure of the spacer layers, while the hole doping by (Fe, Ni) substitution directly distorts the superconducting blocks of the crystal lattice, we can conclude that such changes in the composition do not seriously affect the underlying pairing mechanism in 122-arsenides. A similar scaling between $\Delta_{L,S}$ and T_c was observed by us in iron-based oxypnictides of the 1111 family and 11-selenides [34]. An anisotropy of the small gap was not observed in our experiments, in agreement with most of other studies. The only available ARPES data [21] reported a small gap anisotropy. Of course, this problem requires further experimental studies.

Despite the multi-orbital nature and the presence of at least three interacting bands at the Fermi level, the simple two-band model, as we have shown, suffices for even a quantitative fitting of the temperature dependence of the most important parameters: the large and small gaps, the electron specific heat, and the lower critical field. According to our estimations, two effective bands (where at $T < T_c$ the two condensates are developed with the gaps Δ_L and Δ_S) interact rather weakly. The common T_c value results mainly from a strong intraband coupling in the 'driving' bands, with nonzero Coulomb repulsion being essential for describing the two-gap state of Ba-122 correctly. This indicates that our experimental data seem to disagree with the predictions of the initial $s^{\pm}$ model based on strong interband pairing [15], thus favoring a realization of the s^{++} state [13,14].

9. Conclusions

We have presented a comprehensive study of $BaFe_{2-x}Ni_xAs_2$ and $Ba_{1-x}K_xFe_2As_2$ single crystals with the respective electron and hole doping, belonging to the Ba-122 family of high-temperature superconductors. Despite the different dopant types, both compounds demonstrate similar superconducting properties. The high-quality $Ba(Fe, Ni)_2As_2$ single crystals with various nickel concentrations and critical temperatures up to $T_c \approx 21$ K were synthesized using the self-flux method. The characterization revealed the presence of a single superconducting phase and high homogeneity of the superconducting properties of the crystals studied.

To study the structure of the superconducting order parameter, we used five complementary techniques.

The specific heat and the lower critical field measurements gave information about the bulk properties; intrinsic multiple Andreev reflection effect (IMARE) spectroscopy locally probed the bulk superconducting parameters directly, whereas optical spectroscopy and ellipsometry probed the crystal surface. Nonetheless, the results obtained using the different techniques are in good agreement. The major qualitative conclusion of our studies is the coexistence of two components of the superconducting condensate with unequal electron–boson interactions. The two gaps developed in separate Fermi surface sheets have no nodes in the $k_x k_y$-plane and have an extended s-wave symmetry, in agreement with ARPES data.

Numerical data on the structure of the superconducting order parameter obtained by various techniques can be summarized as follows:

(a) for optimal $Ba_{1-x}(K_x)Fe_2As_2$, the large gap has the amplitude $\Delta_L(0) = 8-11.3$ meV and a $\sim 30\%$ in-plane anisotropy in the $k_x k_y$-plane; the small gap value is $\Delta_S(0) = 1.7-2.5$ meV;

(b) for $Ba_{1-x}(K_x)Fe_2As_2$ and $Ba(Fe_{1-x}Ni_x)_2As_2$, the determined BCS ratios $2\Delta_L/(k_B T_c)$ are close to each other and well above the weak-coupling limit due to a strong intraband electron–boson interaction in the bands with the large gap. The self-consistency of the order parameter structure indicates the invariance of the pairing mechanism in these compounds, despite the different dopant types and different T_c;

(c) as the temperature increases, the large and the small gap, the electron specific heat, and the lower critical field decrease in accordance with a law that is not of the single-band BCS type. Remarkably, the two-band model is apparently sufficient for describing the most important superconducting parameters;

(d) the moderate interband coupling and the significance of nonzero Coulomb repulsion in describing the two-gap superconducting state do not contradict the possible realization of the s^{++} model.

Acknowledgments

We thank M M Korshunov, M Abdel-Hafiez, Y Chen, and P D Grigoriev for the fruitful discussions and the materials provided. T E K, A V M, A V S, V A V, and Yu F E acknowledge the Russian Science Foundation (project no. 16-12-10507) for financial support. S A K, Yu A A, K S P, and V M P acknowledge the Russian Science Foundation (project no. 16-42-01100) for financial support. Yu A A acknowledges support from the MEPhI Academic Excellence Project (contract No. 02.a03.21.0005).

References

1. Kamihara Y et al. *J. Am. Chem. Soc.* **130** 3296 (2008)
2. Fujioka M et al. *Appl. Phys. Lett.* **105** 102602 (2014)
3. Ge J-F et al. *Nature Mater.* **14** 285 (2015)
4. Khlybov E P et al. *JETP Lett.* **90** 387 (2009); *Pis'ma Zh. Eksp. Teor. Fiz.* **90** 429 (2009)
5. Paglione J *Phys. Canada* **67** 85 (2011)
6. Pervakov K S et al. *Supercond. Sci. Technol.* **26** 015008 (2013)
7. Borisenko S V et al. *Symmetry* **4** 251 (2012)
8. Wang C et al. *J. Am. Phys. Soc.* **138** 2170 (2016)
9. Bianconi A *Nature Phys.* **9** 536 (2013)
10. Singh D J *Physica C* **469** 418 (2009)
11. Paglione J, Greene R L *Nature Phys.* **6** 645 (2010)
12. Seidel P *Supercond. Sci. Technol.* **24** 043001 (2011)
13. Onari S, Kontani H *Phys. Rev. Lett.* **103** 177001 (2009)
14. Saito T, Onari S, Kontani H *Phys. Rev. B* **88** 045115 (2013)
15. Maiti S, Chubukov A V *Phys. Rev. B* **87** 144511 (2013)
16. Korshunov M M *Phys. Usp.* **57** 813 (2014); *Usp. Fiz. Nauk* **184** 882 (2014)
17. Charnukha A et al. *Sci. Rep.* **5** 10392 (2015)
18. Abrikosov A A *Physica C* **341–348** 97 (2000)
19. Ding H et al. *Europhys. Lett.* **83** 47001 (2008)
20. Evtushinsky D V et al. *Phys. Rev. B* **89** 064514 (2014)
21. Evtushinsky D V et al. *Phys. Rev. B* **87** 094501 (2013)
22. Aswartham S et al. *Phys. Rev. B* **85** 224520 (2012)
23. Khasanov R et al. *Phys. Rev. Lett.* **102** 187005 (2009)
24. Evtushinsky D V et al. *Phys. Rev. B* **79** 054517 (2009)
25. Charnukha A et al. *Phys. Rev. B* **84** 174511 (2011)
26. Shan L et al. *Phys. Rev. B* **83** 060510(R) (2011)
27. Evtushinsky D V et al. *Phys. Rev. B* **89** 064514 (2014)
28. Daghero D et al. *Rep. Prog. Phys.* **74** 124509 (2011)
29. Samuely P et al. *Physica C* **469** 507 (2009)
30. Hardy F et al. *Europhys. Lett.* **91** 47008 (2010)
31. Pramanik A K et al. *Phys. Rev. B* **84** 064525 (2011)
32. Ren C et al. *Physica C* **469** 599 (2009)
33. Perucchi A et al. *Eur. Phys. J. B* **77** 25 (2010)
34. Kuzmicheva T E et al. *Phys. Usp.* **57** 819 (2014); *Usp. Fiz. Nauk* **184** 888 (2014)
35. Park J T et al. *Phys. Rev. Lett.* **107** 177005 (2011)
36. de la Cruz C et al. *Nature* **453** 899 (2008)
37. Shamoto S et al. *Phys. Rev. B* **82** 172508 (2010)
38. Wakimoto S et al. *J. Phys. Soc. Jpn.* **79** 074715 (2010)
39. Efremov D V et al. *Phys. Rev. B* **84** 180512(R) (2011)
40. Kuzmicheva T E et al. *J. Supercond. Novel Magn.* **29** 3059 (2016)
41. Ricci A et al. *Phys. Rev. B* **91** 020503(R) (2015)
42. Caivano R et al. *Supercond. Sci. Technol.* **22** 014004 (2009)
43. Haberkorn N et al. *Solid State Commun.* **231–232** 26 (2016)
44. Dew-Hughes D *Philos. Mag.* **30** 293 (1974)
45. Stout J W, Catalano E *J. Chem. Phys.* **23** 2013 (1955)
46. Hardy F et al. *Phys. Rev. B* **81** 060501(R) (2010)
47. Popovich Pet al. *Phys. Rev. Lett.* **105** 027003 (2010)
48. Abdel-Hafiez M et al. *Phys. Rev. B* **91** 024510 (2015)
49. Padamsee H, Neighbor J E, Shifman C A *J. Low Temp. Phys.* **12** 387 (1973)
50. Bouquet F et al. *Europhys. Lett.* **56** 856 (2001)
51. Muratov A V et al., arXiv:1612.05540
52. Basov D N, Timusk T *Rev. Mod. Phys.* **77** 721 (2005)
53. Dressel M et al. *IEEE J. Select. Topics Quantum Electron.* **14** 399 (2008)
54. Palmer L H, Tinkham M *Phys. Rev.* **165** 588 (1968)
55. Schafgans A A et al. *Phys. Rev. B* **84** 052501 (2011)
56. Ponomarev Ya G, Uk K K, Lorenz M *IOP Conf. Ser.* **167** 241 (2000)
57. Kuzmicheva T E et al. *Europhys. Lett.* **102** 67006 (2013)
58. Kuzmichev S A, Kuzmicheva T E *Low Temp. Phys.* **42** 1008 (2016); *Fiz. Nizk. Temp.* **42** 1284 (2016)
59. Sharvin Yu V *Sov. Phys. JETP* **21** 655 (1965); *Zh. Eksp. Teor. Fiz.* **48** 984 (1965)
60. Octavio M et al. *Phys. Rev. B* **27** 6739 (1983)
61. Arnold G B *J. Low Temp. Phys.* **68** 1 (1987)
62. Averin D, Bardas A *Phys. Rev. Lett.* **75** 1831 (1995)
63. Kümmel R, Gunsenheimer U, Nicolsky R *Phys. Rev. B* **42** 3992 (1990)
64. Devereaux T P, Fulde P *Phys. Rev. B* **47** 14638(R) (1993)
65. Kuzmichev S A et al. *JETP Lett.* **98** 722 (2013); *Pis'ma Zh. Eksp. Teor. Fiz.* **98** 816 (2013)
66. Bok J, Bouvier J *Physica C* **274** 1 (1997)
67. Moreland J, Ekin J W *J. Appl. Phys.* **58** 3888 (1985)
68. Abdel-Hafiez M et al. *Phys. Rev. B* **90** 054524 (2014)
69. Nakamura H et al. *J. Phys. Soc. Jpn.* **78** 123712 (2009)
70. Ponomarev Ya G et al. *Phys. Rev. B* **79** 224517 (2009)
71. Shan L et al. *Nature Phys.* **7** 325 (2010)
72. Luo Q et al. *Supercond. Sci. Technol.* **21** 125014 (2008)
73. Moskalenko V A *Fiz. Met. Metalloved.* **8** 522 (1959)
74. Suhl H, Matthias B T, Walker L R *Phys. Rev. Lett.* **3** 552 (1959)
75. Rettig L et al. *New J. Phys.* **15** 083023 (2013)
76. Kuzmichev S A, Kuzmicheva T E, Tchesnokov S N *JETP Lett.* **99** 295 (2014); *Pis'ma Zh. Eksp. Teor. Fiz.* **99** 339 (2014)
77. Kuzmichev S A et al. *J. Supercond. Novel Magn.* **29** 1111 (2016)
78. Mazin I I, Schmalian J *Physica C* **469** 614 (2009)
79. Ren C et al. *Phys. Rev. Lett.* **101** 257006 (2008)
80. Carrington A, Manzano F *Physica C* **385** 205 (2003)
81. Luo H G, Xiang T *Phys. Rev. Lett.* **94** 027001(2005)
82. Kuzmicheva T E, Kuzmichev S A, Zhigadlo N D *JETP Lett.* **99** 136 (2014); *Pis'ma Zh. Eksp. Teor. Fiz.* **99** 154 (2014)